Molecular Dynamics Simulations of the Anchoring and Tilting of the Lung-Surfactant Peptide SP-B_{1-25} in Palmitic Acid Monolayers

Hwankyu Lee,* Senthil K. Kandasamy,† and Ronald G. Larson*†‡
Departments of *Biomedical Engineering and †Chemical Engineering, and ‡Mechanical Engineering and Macromolecular Science and Engineering Program, University of Michigan, Ann Arbor, Michigan 48109

ABSTRACT We have performed molecular dynamics simulations of multiple copies of the lung-surfactant peptide SP-B_{1-25} in a palmitic acid (PA) monolayer. SP-B_{1-25} is a shorter version of lung-surfactant protein B, an important component of lung surfactant. Up to 30 ns simulations of 20 wt % SP-B_{1-25} in the PA monolayers were performed with different surface areas of PA, extents of PA ionization, and various initial configurations of the peptides. Starting with initial peptide orientation perpendicular to the monolayer, the predicted final tilt angles average 54°∼ 62° with respect to the monolayer normal, similar to those measured experimentally by Lee et al. (Biophysical Journal. 2001. Synchrotron x-ray study of lung surfactant-specific protein SP-B in lipid monolayers. 81:572–585). In their final conformations, hydrogen-bond analysis and amino acid mutation studies show that the peptides are anchored by hydrogen bond interactions between the cationic residues Arg-12 and Arg-17 and the hydrogen bond acceptors of the ionized PA headgroup, and the tilt angle is affected by the interactions of Tyr-7 and Gln-19 with the PA headgroup. Our work indicates that the factors controlling orientation of small peptides in lipid layers can now be uncovered through molecular dynamics simulations.

INTRODUCTION

Lung surfactant (LS) is a mixture of lipids, fatty acids, and proteins that lines the epithelial cells of mammalian lungs. The main function of LS is to reduce the surface tension at the air-liquid interface during breathing, which stabilizes the interface against collapse (1–3). Dysfunction or absence of LS can lead to respiratory distress syndrome (RDS), which is a leading cause of premature infant death (4). RDS has been clinically treated with a mixture of bovine natural surfactant and synthetic lipids (5,6). Although animal surfactants can be used as replacements for human LS, their supply is limited (7). In addition, they can cause infection or immunological response. The most appropriate method for avoiding these problems is to use synthetic mimics of the natural peptides (8). To help in the development of these, it is important to understand the interactions between surfactant proteins and lipids and how these affect interfacial properties in lungs.

Although experimental methods such as NMR, neutron scattering, and x-ray scattering provide vital information on the ensemble-averaged peptide-lipid interactions, these experiments are not always easy to interpret at the level of individual molecules or specific interactions between proteins and lipids. On the other hand, molecular-level phenomena can be visualized by molecular dynamics (MD) simulations, which offer insights into membrane structure and dynamics, as well as interactions between peptides and membranes, assuming that these simulations can be validated by successful comparisons to available experimental results.

LS consists of 90% lipids such as dipalmitoylphosphatidylcholine (DPPC), unsaturated phosphatidylcholine (PC), phosphatidylglycerol (PG), palmitic acid (PA), and 8–10% surfactant-associated proteins such as surfactant proteins A, B, C, and D (SP-A, SP-B, SP-C, and SP-D) (9). Phospholipids are most responsible for the surface properties in the lung. DPPC, which is a zwitterionic phospholipid, is the major surfactant phospholipid and plays an important role in reducing surface tension by packing tightly at the air-liquid interface. However, the interfacial properties of the phospholipids are critically modulated by surfactant-associated proteins. In particular, it has been thought that SP-B and SP-C, which are small and hydrophobic surfactant proteins, significantly contribute to surface activity by disrupting the ordered bilayers, producing fluid-like structures that can spread along the air-water interface more rapidly (10–17). It is believed that SP-B and SP-C promote selective retention of DPPC and squeeze-out of non-DPPC lipids (such as PG) during monolayer compression, thereby helping monolayers to become enriched in DPPC. However, some recent studies show that absorbed surfactant monolayers and their associated reservoirs possess similar lipid compositions, suggesting that the ability of LS monolayers to attain low surface tension is not dependent on their enrichment in DPPC, thus arguing against the classical model of selective DPPC insertion and PG squeeze-out during surfactant monolayer formation (18,19). In addition, it has been recently demonstrated that disorder in bilayers does not speed up the adsorption of pulmonary surfactant, suggesting that SP-B and SP-C facilitate rapid adsorption of pulmonary surfactant through a mechanism other than the disruption of bilayers (20). SP-B also regulates the processing of SP-C, an LS peptide that apparently plays an important role in formation of the

Submitted May 11, 2005, and accepted for publication August 31, 2005.
Address reprint requests to Ronald G. Larson, E-mail: rlarson@umich.edu.

0006-3495/05/12/3807/15 $2.00
doi: 10.1529/biophysj.105.066241

surfactant reservoir and in the reinsertion of surfactant into the collapsed phase to allow reexpansion during inhalation (21,22). Although SP-B and SP-C directly affect the properties of the phospholipid monolayer, SP-A and SP-D, which are larger, hydrophilic proteins, play minor roles in the surface activity. SP-A- or SP-D-knockout mice do not show signs of respiratory malfunction, whereas SP-B knockout mice exhibit fatal respiratory dysfunction (23). Therefore, understanding the interactions of lipids with SP-B will be important in the development of synthetic LS peptides.

The protein SP-B is relatively small (17.4 kDa), homodimeric, and hydrophobic. Each 79-residue polypeptide chain of SP-B contains three disulfide bridges, and the dimer is formed by a disulfide bond linking the Cys-48 residues of the two subunits (24). It has been demonstrated that a shorter version of the protein, SP-B_{1-25}, which contains 25 amino acids and is not dimerized, has the same effects on the surface properties of the lung as does the whole peptide, including resistance to the inhibitory effect of plasma constituents on surfactant activity and partial restoration of lung compliance in two animal models, as well as good lipid mixing and adsorption activities (25). The sequence of SP-B_{1-25} is FPIPL PYCWL CRALI KRIQA MIPKG. Fig. 1 shows the hydrophobic, cationic, and other hydrophilic regions of SP-B_{1-25}. The first eight residues are highly hydrophobic and are hypothesized to facilitate insertion of the peptide into the lipid monolayer. Residues 9–22 form an amphipathic α-helix, and residues 23–25 form a coil. In Langmuir trough experiments with monolayers of PA, both SP-B and SP-B_{1-25} have been shown to inhibit the formation of condensed phases, resulting in a new fluid phase (27,28). Although PA is a minor component of LS, PA has been demonstrated to be necessary for the proper functioning of both natural and synthetic LS replacement (29). In addition,

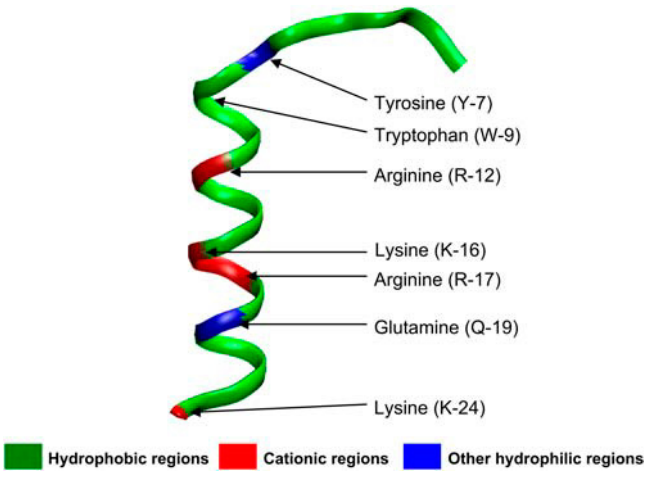

FIGURE 1 Structure of SP-B_{1-25}. The peptide is represented as a ribbon. Red regions represent cationic amino acids, blue regions represent other hydrophilic amino acids, and green regions represent hydrophobic ones. The image was created by using visual molecular dynamics (26).

it was observed that the addition of SP-B_{1-25} increases the collapse pressure of PA monolayers to that of DPPC monolayers (~70 mN/m). This suggests that the electrostatic interactions between the peptide and PA counteract the driving force for the squeeze-out of the fluidizing components such as PG and PA from LS monolayers (30,31). The importance of interactions between PA and SP-B_{1-25} has stimulated diverse qualitative and quantitative measurements of this system by fluorescence microscopy, Brewster angle microscopy, x-ray grazing-incidence diffraction, and reflectivity (27,28,32).

MD simulations have shown that SP-B_{1-25} forms stronger interactions with DPPG lipid monolayers, which are anionic lipids, than with DPPC monolayers, which are zwitterionic (33). Recently, simulations of the interactions between SP-B_{1-25} and DPPC lipid monolayers showed that the polar and cationic amino acids of the peptide form hydrogen bond interactions with headgroups of lipids, suggesting that these hydrogen bonds help determine the position and orientation of the peptide on the interface (34). PA, when deprotonated, has anionic headgroups, which also can form specific interactions with the cationic amino acids of the peptides. Moreover, the headgroup of PA is much smaller than that of DPPC or POPC, making these fatty acids more mobile than two-tailed lipids and hence faster to equilibrate in computer simulations. Furthermore, peptides in PA have much better x-ray contrast than the same peptides in lipids, which allows their orientation and insertion depth to be inferred experimentally. Therefore, SP-B_{1-25} in a PA monolayer is an excellent model for both experiments and simulations to study the conformation and dynamics of LS components.

X-ray diffraction studies of monolayers show the preferred conformation and orientation of SP-B_{1-25} in the PA monolayer, as well as the effect of SP-B_{1-25} on the properties of the PA monolayer (32). Earlier 2.7 ns-long simulations of SP-B_{1-25} in a PA monolayer by Freites et al. (35) indicate that the electrostatic interactions between the cationic peptide residues and the anionic lipid headgroups are prominent and may help anchor the peptide to the monolayer. However, those simulations were performed with initial configurations of the peptide/PA monolayer that were chosen to be the same as final configurations found in the experiment. Thus, simulations that explore different initial peptide orientations and that are run much longer than 2.7 ns are needed to confirm and expand on the findings of this early study. In addition, specific interactions between the peptides and PA should be analyzed at the atomic scale. In this study, we perform 30 ns-long MD simulations to investigate both these atomic-scale interactions between SP-B_{1-25} and PA monolayers as well as larger molecular-scale properties, such as peptide orientation and depth of insertion. Using various initial conditions, we study the effect of the peptide on the monolayer structure and, conversely, the effect of the anionic PA on the conformation and orientation of the peptide and compare our results with experimental findings (32). We are particularly interested

in the effect that individual amino acid residues have on the peptide conformation and on monolayer properties. These results should help in the rational design of synthetic LS peptides.

METHODS

All the simulations and analyses were performed using the GROMACS simulation package with the GROMACS force field (36,37). The united-atom parameter set for lipids was downloaded from http://moose.bio.ucalgary.ca/Downloads and then used for the PA tail. For PA headgroup, parameters for amino acids were used. The peptide structure and coordinates were downloaded from the Protein Data Bank (PDB code: 1DFW) (38). Hydrogen atoms of the PA headgroup and the peptide were fixed by defining an additional bond of appropriate length between the hydrogen atom and the linked atom, which allows the time step to be increased to 5 fs without influencing thermodynamical and dynamical properties of the system (39). The SPC water model was used for all simulations.

Monolayer configuration and equilibration

The simulated system consists of two monolayers with 144 PA molecules in each monolayer, ~6800 water molecules, and counterions to make the system neutral. Several monolayers were constructed with different surface areas, namely, 20 Å^2/PA, 24 Å^2/PA, and 28 Å^2/PA, as well as different proportions of PA ionization, namely, 0%, 25%, 33%, 50%, and 100%. Uniformity in positioning of the ionized and un-ionized PA molecules was achieved by grouping together in the monolayer sets of four PA molecules containing un-ionized and ionized PA in the ratios 4:0, 3:1, 2:2, and 0:4 to make 0%-, 25%-, 50%-, and 100%-ionized PA monolayers. Nine PA molecules were also grouped in the ratio 6:3 un-ionized/ionized PA to make a 33%-ionized PA monolayer. For the monolayer with 24 Å^2/PA, those four or nine PA molecules were replicated, respectively, 36 times or 16 times to make a 144-PA monolayer with the size 5.879 nm × 5.879 nm × 2.2 nm. After duplicating this 144-PA monolayer, the two monolayers were placed face-to-face, parallel to the *xy* direction, and the distance between headgroups of the two monolayers was set to 6 nm; ~6800 water molecules were placed between the hydrophilic faces of the monolayers in a box of size 5.879 nm × 5.879 nm × 6 nm. Na^+ and Cl^- ions were added in positions that minimize electrostatic energy. Enough ions were added both to neutralize charges from the PA and peptide and to create a concentration of 150 mM NaCl. Periodic boundary conditions were applied in all three directions. A region of vacuum with dimensions 5.879 nm × 5.879 nm × 5 nm was introduced above the tail region of the upper monolayer and below the tail region of the lower monolayer to separate the tail regions of the two monolayers from each other in the periodic box. For densities of 20 and 28 Å^2/PA, the same procedures were performed with different box dimensions.

Table 1 shows the parameter values chosen for each step of the simulations. A cutoff was used for van der Waals interactions, and particle mesh Ewald (PME) summation was used for electrostatic interactions (40). The temperature was maintained at 298.15 K by applying a Berendsen thermostat (41). An NVT ensemble was used to fix the surface areas of PA; therefore, the pressure fluctuated during the simulations. After energy minimization, equilibration runs were performed for 10 ns during which no water or counterions were observed to penetrate through the PA tails into the vacuum region. The final PA configurations were analyzed for the pure monolayer and then used as the starting states for inserting the peptide into the monolayer.

Peptide insertion and equilibration

Peptides were inserted into the equilibrated monolayers obtained from step 1, using methods similar to what we have reported earlier (34). Briefly, a hole for inserting peptides was made by following the well-established ''hole'' protocol (42). The ''MSMS'' program was used for scanning the surface of peptides (43), and then a hole-making force was introduced perpendicularly to the scanned surfaces of the peptide. The peptide was inserted into the resulting hole, and then several steps of energy minimization were performed with position restraints applied to the peptide. To attain the desired concentration of peptides in the PA monolayer, namely, 20 wt % SP-B_{1-25}, three peptides were added to each monolayer, requiring prior removal of nine PA molecules and the associated counterions for the charged PA molecules. Removal of nine PA molecules per monolayer leads to an increase in surface area per PA from 24 and 28 Å^2/PA to 25.6 and 29.9 Å^2/PA, respectively. With the added peptides, counterions were added into the water to neutralize the system. Thus, the final system consists of 6 peptides, 270 PA molecules, ~6800 water molecules, and 62, 128, and 332 ions for 0%-, 25%-, and 100%-ionized PA monolayers, respectively. Then, the backbone atoms of the peptide were position restrained, and an equilibration run of 0.5 ~ 1 ns was performed under the conditions listed in Table 1 to allow the PA molecules to equilibrate around each peptide. The final configuration from this equilibration run was used as the starting condition for the production runs. The peptides were inserted in several different initial configurations, listed in Table 2 and Fig. 2, to test for equilibration of the system.

TABLE 1 Simulation parameters for each step; all simulations were performed in the NVT ensemble

	PA equilibration	Peptide insertion	Peptide-PA equilibration	Production run
Temperature (K)	298.15	298.15	298.15	298.15
VdW cutoff (nm)	1.2	1.2	1.2	1.2
Electrostatics	PME	PME	PME	PME
Length of the run (ns)	10	0.01	0.5 ~ 1	30
Position restraints	-	Carbon atoms next to PA headgroups in the *x*, *y* plane	Peptide backbone	-
Position restraint force (kJ/mol/nm^2)	-	1000	1000	-
Hole-making force (kJ/mol/nm)	-	100	-	-

Production runs

MD simulations of SP-B_{1-25}/PA monolayer systems prepared using the above procedure were carried out with parameter values listed in Table 1. Using the NVT ensemble, the surface area of PA was fixed at 25.6 or 29.9 Å^2/PA, and the pressure was allowed to fluctuate. As in the preparation steps, the temperature was maintained at 298.15 K by applying a Berendsen thermostat, a cutoff was used for van der Waals interactions, and PME summation was used for the electrostatic interactions. The LINCS algorithm was used to constrain the bond lengths (44). The simulations were performed for 30 ns with a time step of 2.5 ~ 5 fs. The coordinates were saved every picosecond for analysis.

RESULTS AND DISCUSSION

Peptide-free simulations

Experimentally, monolayer electrostatics and ionic strength of the buffer play an important role in determining the phase behavior of the lipid monolayer. A certain proportion of carboxyl groups in the headgroups of PA are ionized at pH 6.9 (the estimated pH of water containing 150 mM NaCl),

TABLE 2 List of simulations; note that in SPB3, the ionized PA molecules are initially placed randomly within the monolayer

Name	Ensemble	Area per PA (Å^2/PA)	Extent of ionization in PA (%)	Distribution of ionized PA	Numbers of peptides with tabulated initial angle formed by helix with monolayer normal			Total simulation time (ns)
					0°	45°	90°	
SPB1	NVT	25.6	0	Spatially regular	6	-	-	30
SPB2	NVT	25.6	25	Spatially regular	6	-	-	30
SPB2-MUT1*	NVT	25.6	25	Spatially regular	6	-	-	30
SPB2-MUT2*	NVT	25.6	25	Spatially regular	6	-	-	30
SPB2-MUT3*	NVT	25.6	25	Spatially regular	6	-	-	30
SPB3	NVT	25.6	25	Spatially random	6	-	-	30
SPB4	NVT	25.6	25	Spatially regular	4	-	2	30
SPB5	NVT	25.6	25	Spatially regular	-	6	-	30
SPB6	NVT	25.6	25	Spatially regular	2	-	4	30
SPB7	NVT	25.6	25	Spatially regular	-	-	6	30
SPB8	NPT	25.6	100	Spatially regular	6	-	-	30
SPB9	NVT	29.9	25	Spatially regular	6	-	-	30

*SPB2-MUT1, SPB2-MUT2, and SPB2-MUT3 are mutated peptides.

which can affect the properties of the PA monolayer. The extent of ionization of the PA monolayers at pH 6.9 (in saline buffer at 0.15 M NaCl) has been shown by the Gouy-Chapman theory to vary from 24% at 17 Å^2/PA (16°C), which is the area per PA at which collapse of the PA monolayer occurs below the triple point, to 39% at 40 Å^2/PA, which is the area per PA for the expanded-to-condensed phase transition of the PA monolayer above the triple point (28°C) (28). Therefore, we have chosen a 25%-ionized PA monolayer as a reference ionization condition to use in our simulations. We have performed a series of 10 ns simulations of pure monolayers containing 288 PA molecules, at densities of 20 Å^2/PA, 24 Å^2/PA, and 28 Å^2/PA, along with ~6800 water molecules and counterions.

Peptide simulations

We have performed MD simulations of 6 SP-$B_{1\text{-}25}$ molecules (3 per monolayer) and 270 PA molecules (135 per monolayer) with different initial configurations of the peptide, surface areas of PA, and extent of PA ionization. Table 2 shows the different initial conditions of all the simulations. The simulations were performed for 30 ns at surface densities of 25.6 Å^2/PA or 29.9 Å^2/PA in an NVT ensemble. Fig. 2 shows snapshots from the beginning (*top image*) and end of all the simulations (*bottom image*). Final conformations show that the peptides become highly tilted and interact strongly with PA molecules. The observed average tilt angles of the peptides in each monolayer correspond reasonably closely to the angles determined experimentally by Lee et al. (32). Although the simulations were performed over a run time of 30 ns, the average properties were analyzed only over the last 10 ns when the system is in its most equilibrated state.

In Fig. 3, *a–d*, mass densities of the peptide and PA tail and head regions are plotted for the pure PA monolayer and the monolayer containing PA-SP-$B_{1\text{-}25}$. In the presence of the peptide, the PA tail and head regions become much broader than in the pure PA monolayer. This occurs because the strong interactions of PA molecules with the peptides can pull PA molecules out of the monolayers. In Fig. 3, *c* and *d*, the breadth of the PA head region matches that of the peptide region, suggesting a strong interaction between the peptide and the PA head region.

The effect of SP-$B_{1\text{-}25}$ on fluidization of the PA monolayer

SP-$B_{1\text{-}25}$ inhibits the formation of condensed phases in monolayers of PA, resulting in a disordered, fluid, monolayer phase (27,28). The PA tail conformational order can be quantified by the order parameter Scc.

$$\mathrm{Scc} = \frac{3}{2}\langle \cos^2 \theta_Z \rangle - \frac{1}{2}$$

where θ_Z is the angle that the vector connecting carbons C_{n-1} to C_{n+1} makes with the z axis. The bracket indicates averaging over time and over all molecules in the simulation. Order parameters can vary between 1 (perfect orientation in the interface normal direction) and $-1/2$ (perfect orientation perpendicular to the normal) (45).

Fig. 4, *a* and *b*, shows the order parameters of the pure PA monolayer with different extents of PA ionization and surface areas. In Fig. 4 *a*, the order parameters of the PA tails are almost identical for ionizations in the range 0% ~ 50%, showing that this level of ionization does not affect the ordering of the monolayer. However, the order parameters of 100%-ionized PA are much reduced, showing that the 100%-ionized PA monolayer is much more disordered. This occurs because of interfacial fluctuations, which are driven by repulsive forces between negatively charged headgroups of PA molecules. In Fig. 4 *b*, the monolayer at a surface density

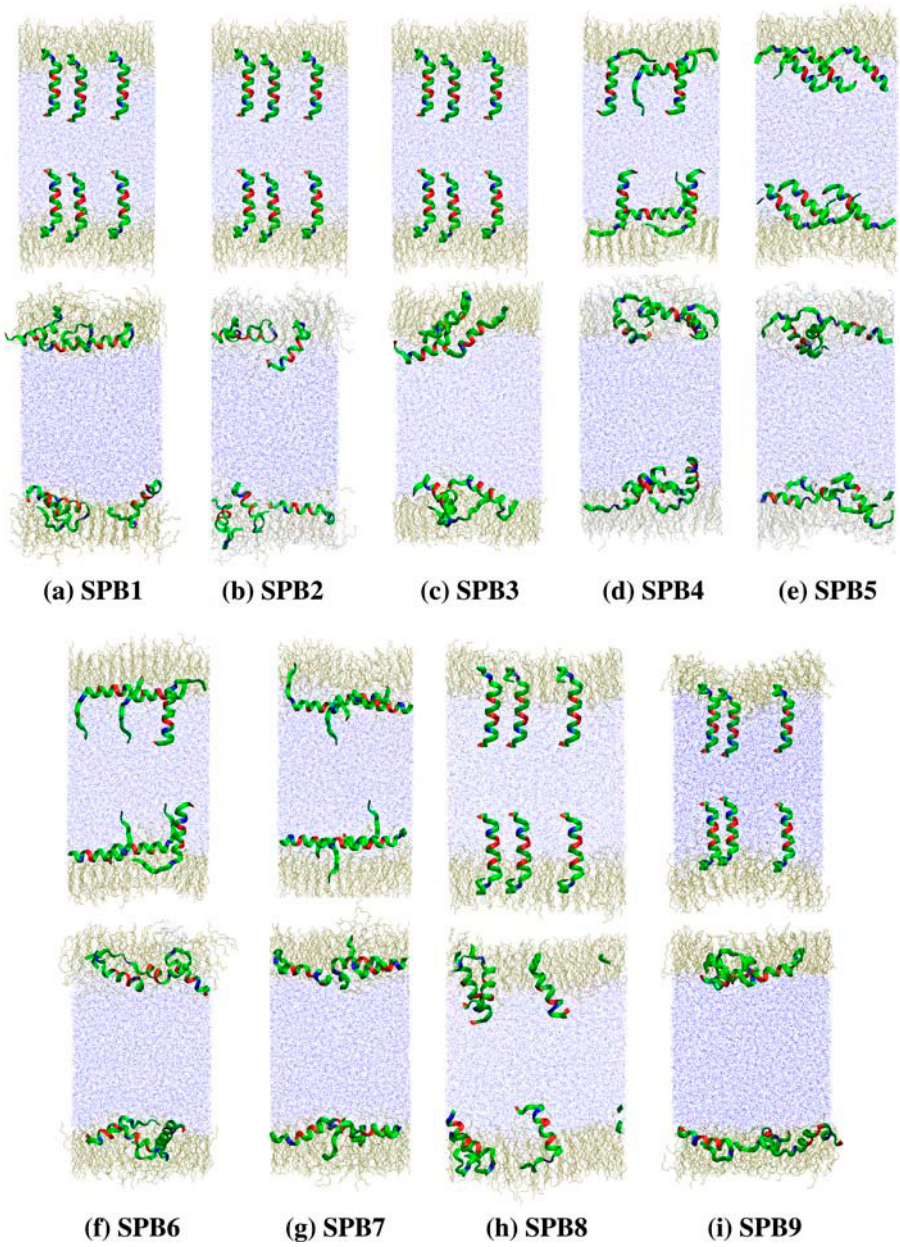

FIGURE 2 Snapshots at the beginning (0 ns, *top image* for each of parts *a–i*) and end (30 ns, *bottom image*) of all the simulations. PA molecules are positioned on the top and bottom of the system. Three peptides for each monolayer are oriented perpendicularly or horizontally with respect to the monolayer normal. Water molecules between monolayers are represented as blue dots. Vacuum is introduced above the upper monolayer and beneath the lower monolayer to avoid interactions between monolayers across the periodic boundary condition. One system contains six peptides, 270 PA molecules, and ~6800 water molecules. All simulations were performed for 30 ns. The final conformations of the systems show that peptides become more tilted and interact more intimately with the monolayers as time increases.

of 28 Å^2/PA is more disordered than at 24 Å^2/PA, probably because there is more space in the former for reorientation of PA molecules. However, the monolayer at 20 Å^2/PA is more disordered than that at 24 Å^2/PA, presumably because of fluctuations of the interface caused by the strong repulsive force between the tightly packed PA molecules. In addition, the fifth carbon close to the headgroup is more disordered than other carbons close to the headgroup. In Fig. 4 *b*, when the surface area of PA is 28 Å^2/PA, the fifth carbon is more disordered, whereas when the surface area of PA is 20 Å^2/PA, this disordering of the fifth carbon rarely occurs. This disordering of the fifth carbon is robust at the higher surface area, since we also found disorder of the fifth carbon in simulations of a monolayer of a shorter PA tail (10 carbons), similar to the disorder of a normal PA tail. We also heated up the PA system to 350 K and then cooled it down to 298 K, and similar behavior of the fifth carbon was found. Experimental measurement of the order parameter of PA would allow this predicted specific disordering to be confirmed, unless it is an artifact of the force fields. The possibility of such an artifact cannot be ruled out at this point because force fields of lipids have been parameterized based on bilayers, not monolayers.

We also calculated the order parameters of PA monolayers in the presence of peptides. Each PA monolayer is divided into two regions based on the distance from the peptide molecules. If any part of a PA molecule is within 5 Å of the surface of the peptide, it is considered to be ''close'' to the

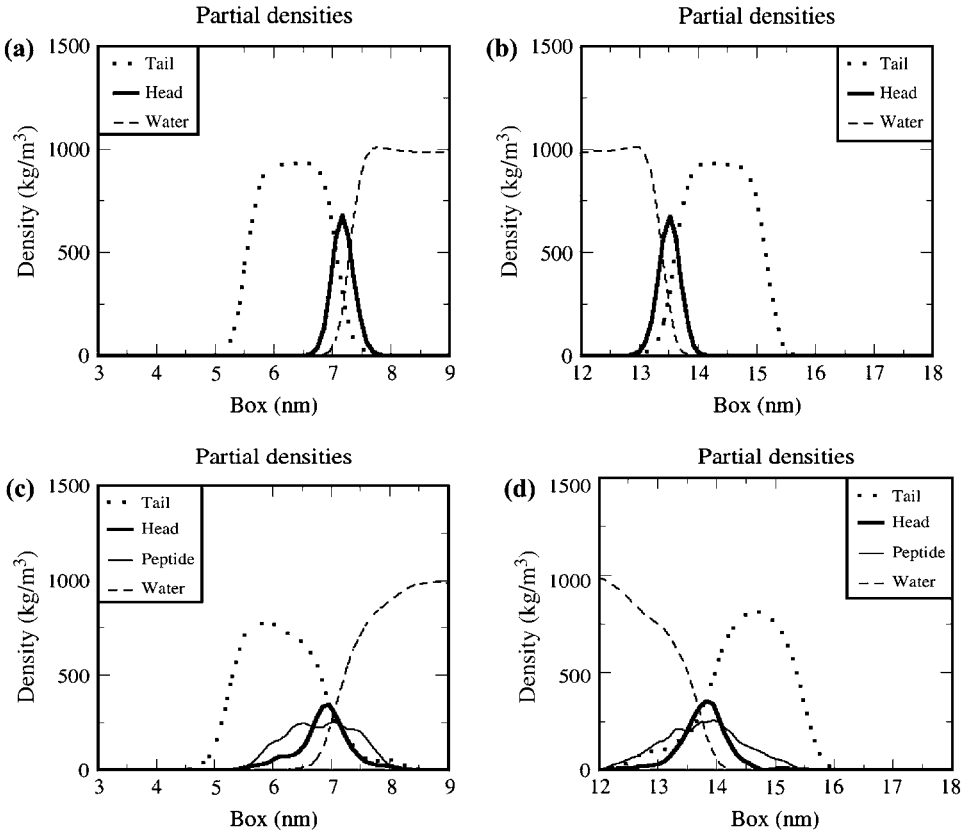

FIGURE 3 Mass density profiles of (*a*) the lower layer and (*b*) the upper layer of the pure PA monolayer, and (*c*) the lower layer and (*d*) the upper layer of the PA-SP-$B_{1\text{-}25}$ monolayer.

peptide, whereas otherwise it is ''far'' from the peptide. Using this criterion, each monolayer consists of 75 ~ 80 PA molecules close to each peptide and 55 ~ 69 PA molecules far from any of the peptides. Fig. 4, *c* and *d*, shows order parameters of PA in the SPB2 system, which is 25%-ionized with a density of 25.6 $Å^2$/PA. Notice that in the vicinity of the peptides there is significant disordering of PA relative to pure PA monolayers, and that there is less disordering for PA molecules far from the peptides. This disordering is consistent with experimental observations, which show that the insertion of the peptides disrupts and disorders the membranes, causing the formation of a novel disordered fluid phase (27,28). In the experiments, the disordered phase is in equilibrium with an ordered phase whose molecular packing is not affected by the peptide (32), suggesting that the peptide is only located in the disordered portion of the monolayer. (In the simulations, the patch of monolayer is too small to allow clear phase separation between disordered and order surface phases.) Notice that in the simulations the PA molecules far from the peptide, although less disordered than those close to the peptide, are nevertheless more disordered than those in the pure PA monolayer. This disordering apparently occurs because PA molecules tend to condense near the peptides to interact intimately with them, leading to an increased surface area of the remaining PA molecules, even those far from the peptide.

Secondary structures and orientation of SP-$B_{1\text{-}25}$ in the PA monolayer

SP-$B_{1\text{-}25}$ consists of an α-helical structure, whose stability in the PA layer and angle relative to the monolayer normal we here investigate. The peptides in the monolayers at 25.6 $Å^2$/PA are observed to have a stable α-helical structure extending from the 8th residue, cysteine, to the 21st residue, methionine. On the other hand, in the monolayers at 29.9 $Å^2$/PA the α-helical structure only extends from the 10th residue, leucine, to the 15th residue, isoleucine, showing that at this lower packing density the α-helical structure is less stable. The 16th residue, lysine, at 29.9 $Å^2$/PA is observed to form only a coil. This result corresponds to simulations performed by Freites et al., which show instability of the α-helical structure to formation of a more random conformation at around the 16th or 17th residue (35). The α-helical structure in the monolayer with a higher surface area is apparently less stable because of the exposure of the peptide to more water molecules. For the peptide in pure water, the α-helix is broken after 300 ps, apparently by the presence of the water molecules.

Lee et al. measured peptide orientation by constructing a four-box model representing the electron densities of the composite objects, peptide-water, peptide-PA head, peptide-PA tail, and PA tail groups, derived from x-ray reflectivity data (32). From this, they inferred that the average peptide

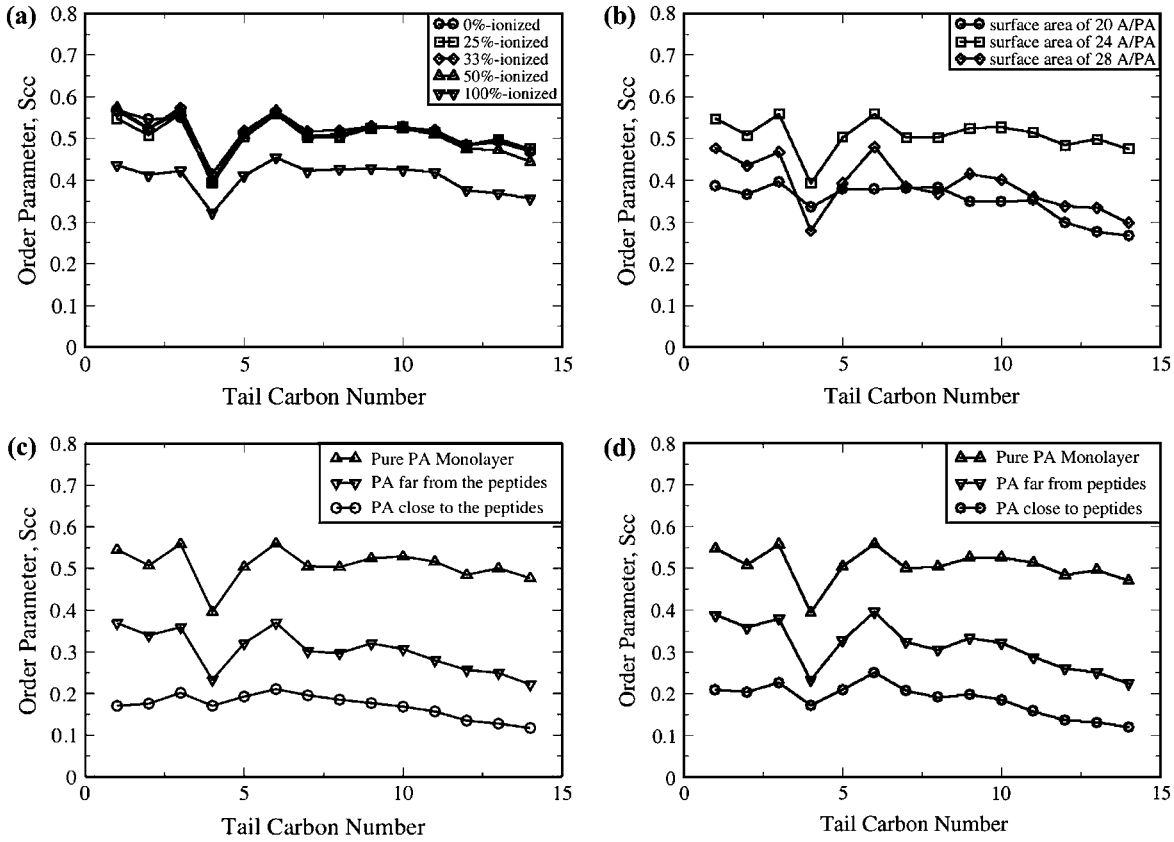

FIGURE 4 Order parameters of acyl chains of PA. The order parameters of pure PA monolayers were measured for (*a*) different extents of PA ionization at a surface area of 24 Å^2/PA and (*b*) different surface areas of PA in a 25%-ionized PA monolayer. The order parameters of PA in SPB3, which initially had all perpendicular peptides, were measured for (*c*) lower and (*d*) upper layers. Each monolayer of SPB3 is divided into two regions including an area far from the SP-$B_{1\text{-}25}$ and the remaining area close to the peptides.

tilt angle was 56°. In our simulations, we investigate the conformations of the peptides by measuring directly the tilt angle, which we define as the angle between the monolayer normal and the α-helical axis of the peptide (Fig. 5 *a*), where the α-helical axis is given by the 8th–21st residues of the peptide. Specifically, to define this axis, the center of mass of the aggregate of atoms consisting of the backbone atoms for the 8th $\sim$ 10th residues and two backbone atoms (N and Cα) of the 11th residue is calculated. Likewise, the center of mass of the backbone atoms of the 19th $\sim$ 21st residues and two backbone atoms (Cα and C) of 18th residues is also calculated, and the line connecting these two centers of mass is used to measure the tilt angle.

Fig. 5, *b* and *c*, shows the time dependencies of the tilt angles of six peptides over a period of 30 ns, in simulations SPB2 and SPB4. Each peptide was initially positioned perpendicularly or horizontally with respect to the monolayer normal as described in Fig. 2 and Table 2. In simulations SPB2 and SPB3, all peptides started vertically (0°). Note that the tilt angles increase rapidly for 10 ns, and little systematic change is observed after 20 ns. In Fig. 5 *c*, for simulation SPB4, four peptides start vertically and two start horizontally. Although the four initially vertical peptides show drastic changes in orientation, similar to the peptides in simulations SPB2 and SPB3, the orientations of the two initially horizontal peptides do not show large changes and merely fluctuate around 90°. This stability of the horizontal peptides is apparently produced by the hydrogen bonds that form between the peptides and the headgroups of the PA molecules. Early formation of hydrogen bonds can prevent the free movement of the peptides, which leads to restricted conformational sampling (34). Lack of free movement of the peptides shows the limitation of simulations over timescales of tens of nanoseconds, which is too short to break hydrogen bonds frequently enough to overcome local energy minima and allow the peptide to sample thoroughly configuration space. This trend is also observed in simulations SPB5, SPB6, and SPB7, showing that tilt angles merely fluctuate around 90°, similar to the peptides that started horizontally in simulation SPB4.

Fig. 5 *d* shows the instantaneous tilt angles averaged over all six peptides from each monolayer system. Although tilt angles of the individual peptides are observed to fluctuate in Fig. 5, *b* and *c*, the tilt angles averaged over six peptides have smaller fluctuations and yield nearly constant angles after 20 ns. Therefore, the average tilt angles of the final conformations

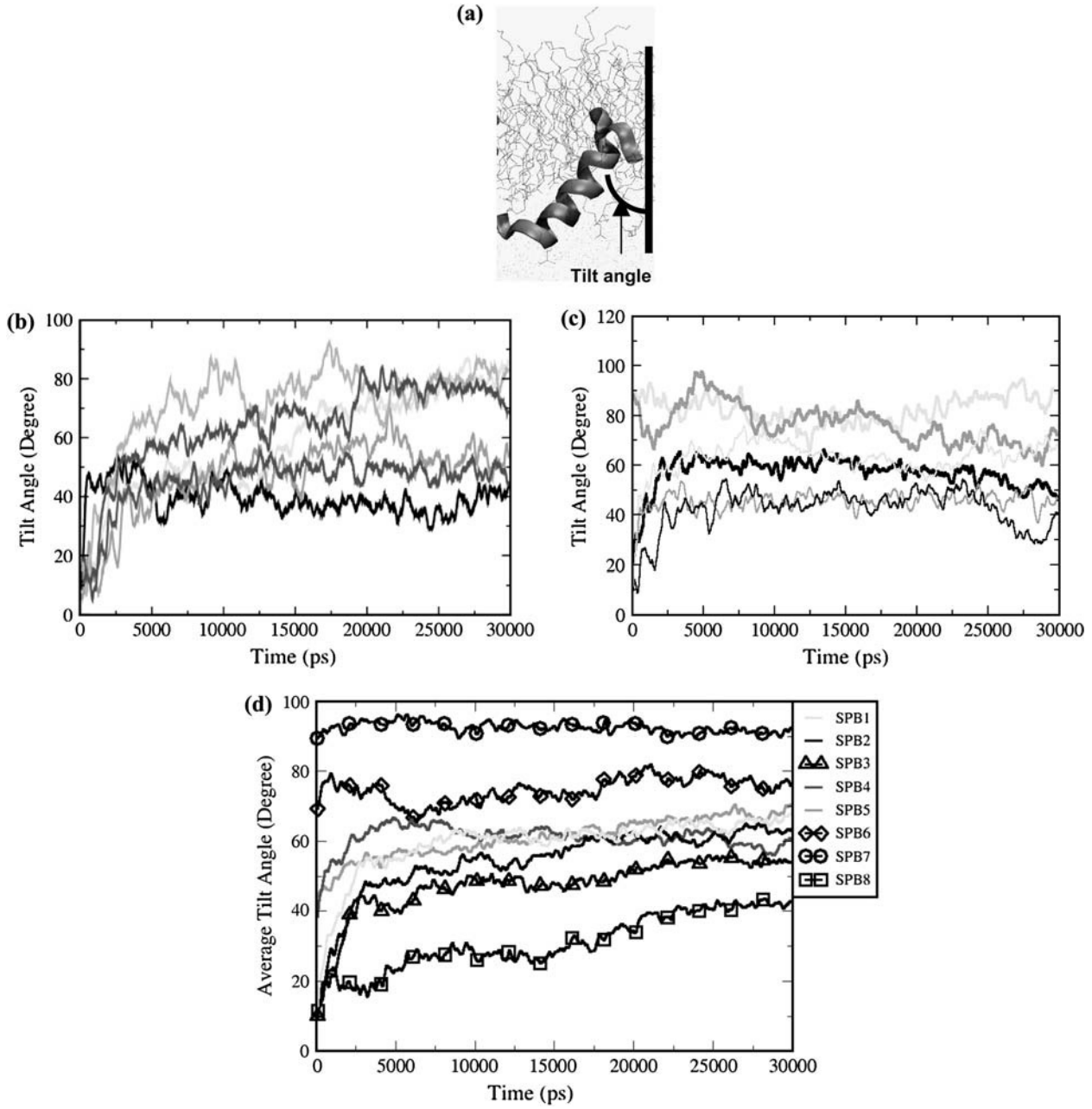

FIGURE 5 Peptide tilt angle (*a*), computed by measuring the angle between α-helix of the peptide and the *z* axis, with 0° representing a vertical orientation and 90° a horizontal one. Tilt angles of the individual peptides in (*b*) SPB2 and (*c*) SPB4. (*d*) Tilt angles averaged over all six peptides of each simulation as a function of simulation time.

were analyzed between 20 ns and 30 ns in all simulations, and the results were tabulated in Table 3. Although for each simulation the peptide tilt angles span a broad range of values, in simulations SPB2, SPB3, and SPB4, these average peptide tilt angles are nearly the same, ranging only from 54° to 62°. Those angles are similar to the experimental value of 56° obtained from the x-ray reflectivity experiments by Lee et al. (32). On the other hand, simulation SPB5 has a final average tilt angle of 67°, SPB6 has 78°, and SPB7 has 91°, which are much higher than the other simulation results and the experimental value. These higher average tilt angles occur because of the limited conformational sampling by the horizontally inserted peptides, as discussed in the analysis of the tilt angles of individual peptides.

In addition to the direct measurement of the peptide tilt angle, we calculated peptide orientation by constructing a four-box model of computed electron densities, mimicking the four-box model fitted to experimental electron densities by Lee et al. (32). The average tilt angles of the peptides obtained from the four-box models fitted to the simulated

TABLE 3 Average tilt angles of SP-B_{1-25} averaged over the time period 20–30 ns for each of six molecules in each system (column 2), and over all six molecules over this period (column 3), for systems with different initial conditions

	Range of tilt angle (°)	Average tilt angle (°)
SPB1	48 ~ 81	65
SPB2	37 ~ 77	62
SPB3	39 ~ 70	54
SPB4	42 ~ 86	60
SPB5	34 ~ 82	67
SPB6	48 ~ 124	78
SPB7	73 ~ 112	91
SPB8	29 ~ 72	41
Experiment (32)		56

electron density profiles are in the range 52–70°, similar to the range of angles obtained from the four-box model fitted to the experiments. For the simulations, where the peptide was initially vertical the fits to four-box models yielded orientation angles of 52–55°, much closer to those calculated directly from the orientation of the α-helical region, which were in the range 54–62°. However, for initially horizontal peptides, the directly calculated tilt angle was ~90°, whereas that from the four-box model was ~70°. These results indicate that fits to four-box models are not sensitive to orientation angles >~70° and that our simulation results, although not completely converged, do yield orientation angles consistent with experimental results, to within the accuracy of the experiments.

In addition to the simulations of the PA monolayers with 20 wt % SP-B_{1-25}, PA monolayers with 7 wt % SP-B_{1-25}, which corresponds to one peptide per monolayer, were also simulated. Fig. 6 shows the tilt angles of the peptides in three such simulations with different initial configurations. Tilt angles change rapidly for the first 5 ns and then become stable after ~15 ns, which is similar to the behavior seen in the 20 wt % SP-B_{1-25} systems. In Fig. 6 *c*, the peptides, which were initially horizontal, stay horizontal, which is similar to the earlier results from the PA monolayers with 20 wt % SP-B_{1-25}. Table 4 shows the average tilt angles of the peptides between 15 and 20 ns in the simulations with one peptide. When the initial tilt angles of the peptides are between 0° and 65°, the final tilt angles end up between 33° and 65°. On the other hand, initially horizontally oriented peptides have average final tilt angles of 86° ~ 96°. This behavior is similar to that of systems with 20 wt % SP-B_{1-25}, suggesting that changes in concentration up to 20 wt % SP-B_{1-25} do not significantly affect the tilt angle, at least over the timescales of these simulations.

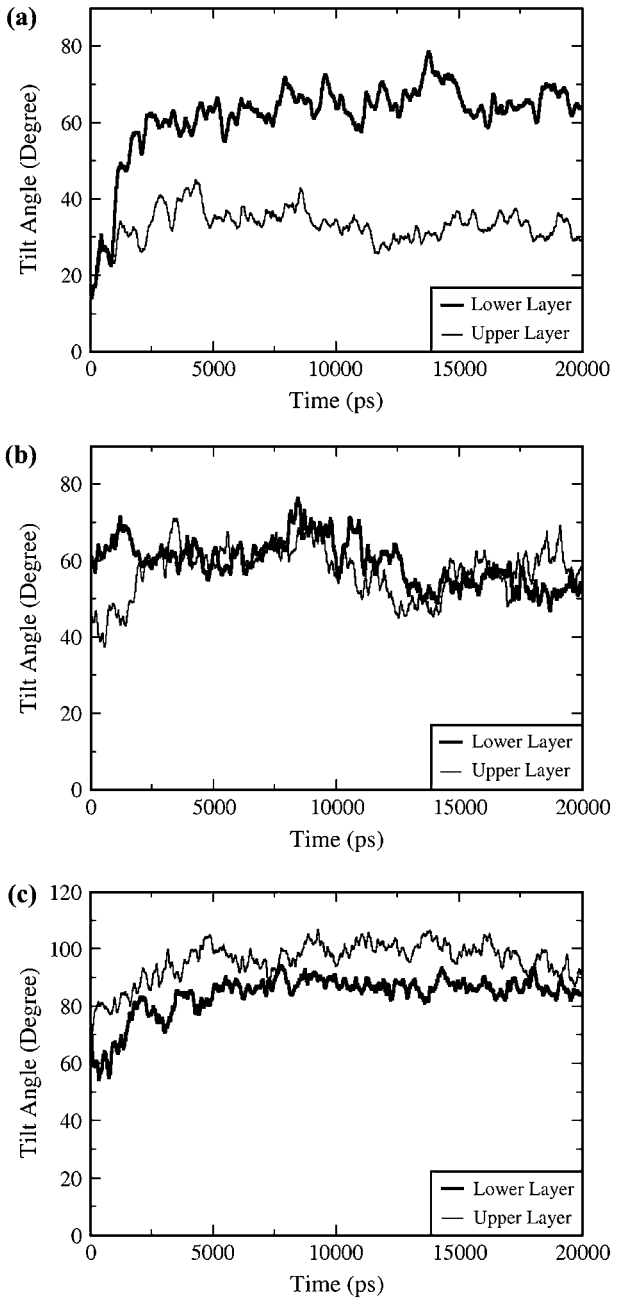

FIGURE 6 Tilt angles of the peptides in the PA monolayers having one peptide with initially (*a*) vertical, (*b*) 50°-tilted, and (*c*) horizontal orientation, 90°. The peptides with initially vertical configuration tend to tilt toward the monolayer, whereas the peptides with initially horizontal orientation remain horizontal.

Hydrogen-bonding interaction between SP-B_{1-25} and PA monolayers

Although the PA tail region consists of uncharged hydrophobic hydrocarbon chains, the headgroup region of PA has a negatively charged carboxyl group, which can form hydrogen bonds with the peptides, particularly with the cationic amino acids. These hydrogen bonds play an important role in determining the final conformation of the peptide in the monolayers. Here, we investigate the specific effects that different amino acids, and their different hydrogen-bonding patterns, have on the orientation and conformation of the peptide. Although the peptide backbone donors have the ability to form hydrogen bonds with the PA

TABLE 4 Tilt angles of peptides in PA monolayers having one SP-B_{1-25}

Initial tilt angle		Final tilt angle (15 ~ 20 ns)	
Lower layer	Upper layer	Lower layer	Upper layer
0	0	65	33
65	47	54	58
73	83	86	96

headgroups, these hydrogen bonds are less significant than those of the side chains, because most peptide backbone donors are used up in forming the helical backbone structure and also are less accessible to the PA than are the side chains (34). Therefore, we only analyze the hydrogen-bonding characteristics of the side chains of the SP-B_{1-25} peptide. The amino acids of SP-B_{1-25} that have side chains with hydrogen-bonding capabilities are tyrosine 7 (Y-7), tryptophan 9 (W-9), arginine 12 (R-12), lysine 16 (K-16), arginine 17 (R-17), glutamine 19 (Q-19), and lysine 24 (K-24). Tyrosine has one donor and one acceptor, the latter being an uncharged, but polar, hydroxyl group, and glutamine has two donors and one acceptor, the latter being an uncharged, but polar, side chain. Arginine and lysine have five and three donors, respectively, due to their charged side chains, which can make hydrogen bond interactions with the anionic headgroups of ionized PA molecules. Tryptophan has one donor with an indole ring joined to a methylene group, which makes tryptophan highly hydrophobic. These donors and acceptors were analyzed to determine the number and duration of hydrogen-bonding interactions, which play an important role in determining the conformation of the peptide in the monolayer.

We base the criterion for the existence of hydrogen bonds on the distance between the donor and the acceptor, and the angle formed by the donor, the acceptor, and the hydrogen. Specifically, we assume that a hydrogen-bonding interaction exists when the hydrogen-acceptor distance is <0.25 nm and the angle of the donor-hydrogen-acceptor triplet is $>120°$ (46). Analyses were performed using different distance and angle criterions, including 0.2 nm-150° and 0.25 nm-150°, which showed that these stricter criteria produce similar qualitative trends (34). Therefore, the 0.25 nm-120° criterion was used for our hydrogen-bonding analysis of all the simulations.

Fig. 7, *a* and *b*, shows hydrogen bond existence maps for Y-7 and K-16 in simulation SPB2 with 25%-ionized PA. Fig. 7 *a* shows the hydrogen bond existence map of Y-7, which has one donor and one acceptor that can make hydrogen bonds with acceptors or donors of the headgroups in PA molecules. The scheme in Fig. 7 *a* shows that, during the course of the simulation, Y-7 makes 14 unique hydrogen bonds (numbers of unique acceptor-donor sites in hydrogen bond map) with ionized or un-ionized PA molecules, which are in the vicinity of the peptide. Note that the side chains of the peptide will not be able to interact with distant PA molecules because of the low diffusivity of the PA molecules and the short simulation timescale. Since Y-7 was initially located in the hydrophobic tail region of the monolayer, hydrogen bonds between the peptide and PA are unlikely to occur at the beginning of the simulation. After 20 ns of simulation, one persistent hydrogen bond (the 13th row of unique acceptor-donor sites in the map) forms, showing that an acceptor of Y-7 makes a strong hydrogen bond with a donor of one un-ionized PA. This trend is also observed in Q-19, which has two donors and one acceptor. Q-19 was initially positioned in the water phase and forms hydrogen bonds with the PA molecules after ~9 ns. The acceptor of Q-19 forms an interaction with the donor of a un-ionized PA molecule, and a donor of Q-19 forms an interaction with an acceptor of either an ionized or a un-ionized PA. Therefore, both Y-7 and Q-19 have interactions with donors or acceptors of PA, suggesting that they can interact with both un-ionized and ionized PA.

Fig. 7 *b* shows that the three cationic donors of K-16 can form three hydrogen bonds with the anionic headgroups of ionized PA molecules. In K-16, frequent breaking and reforming of the same set of three hydrogen bonds is observed apparently because the three hydrogen atoms of the amine group in lysine compete for the same acceptor, causing symmetric rotation around the acceptor of the closest PA. In K-24, a similar rotation among three hydrogen bonds is observed again due to the symmetrical rotation of three hydrogens. However, in simulation SPB-1, there are no persistent interactions between K-16, K-24, and the 0%-ionized PA monolayer, suggesting that lysine preferentially interacts with ionized PA molecules. These trends are also observed in R-12 and R-17. The five cationic donors of R-12 can form five persistent hydrogen bonds with the anionic headgroups of ionized-PA molecules, whereas R-12 does not form hydrogen bonds with 0%-ionized PA monolayer (simulation SPB1). R-12 forms five persistent hydrogen bonds, whereas R-17 forms only two persistent hydrogen bonds with ionized PA molecules, apparently because R-17 is not in the PA headgroup region, and thus there are fewer ionized PA molecules around R-17. W-9 does not form interactions with either ionized or un-ionized PA because tryptophan has a bulky side chain, which can block the hydrogen-bonding site. These hydrogen bond studies confirm the inference of Freites et al. (35) from short MD simulations that the cationic residues of SP-B_{1-25} help anchor the peptide to the PA monolayer.

The effect of hydrogen-bonding interaction on the conformation of SP-B_{1-25}

Fig. 8, *a* and *b*, shows the total number of hydrogen bonds for each peptide in simulations SPB2 and SPB7. In simulation SPB2, all peptides are initially oriented vertically, and the final average tilt angle is ~62°. On the other hand, in simulation SPB7, all the peptides are initially oriented

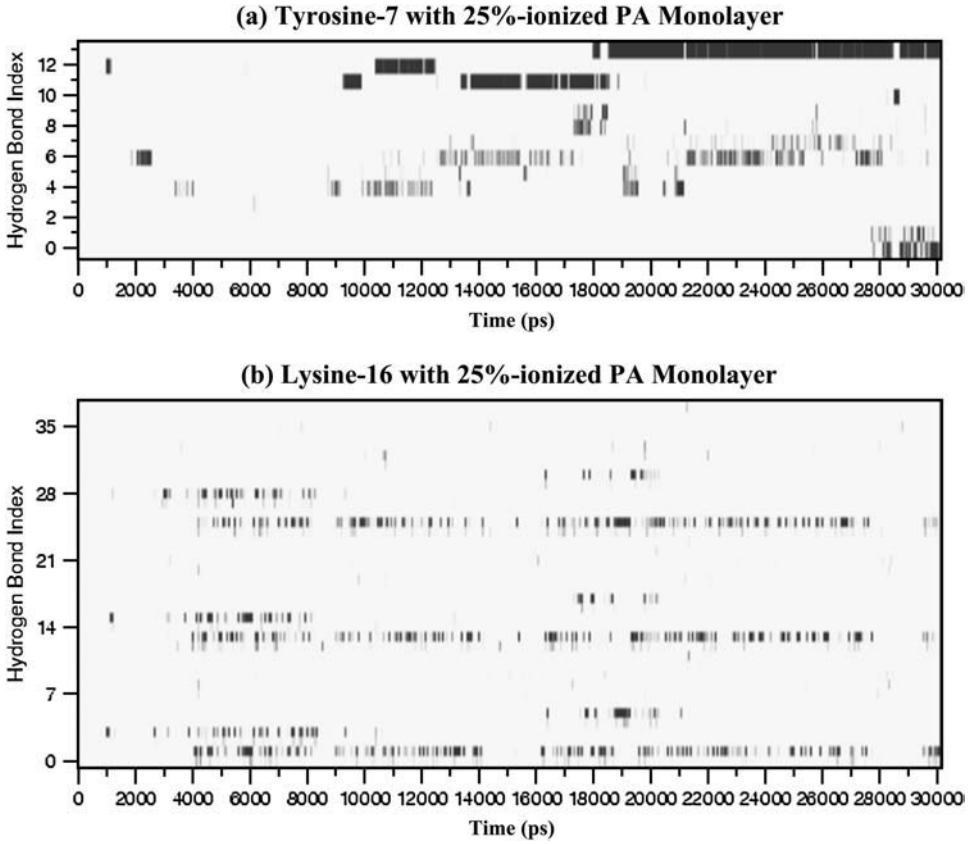

FIGURE 7 Hydrogen bond existence maps for (*a*) tyrosine 7 with 25%-ionized PA and (*b*) lysine 16 with 25%-ionized PA.

horizontally, and the final average tilt angle is ~91°. In Fig. 8 *a*, the numbers of hydrogen bonds increases slowly until 10 ~ 15 ns and eventually levels out, whereas in Fig. 8 *b* leveling out occurs earlier because in the latter, the initial parallel peptide orientation allows hydrogen-bonding pairs to be created more rapidly. Note that the final number of hydrogen bonds is similar for each orientation, suggesting that an equilibrium number has been formed. This large number of hydrogen bonds that form rapidly in the initially parallel orientation apparently pins the peptide in this orientation and therefore might be partially responsible for the lack of change in the tilt angles of the peptides in SPB7.

We analyzed quantitatively the average lifetime of the hydrogen bonds from the integral of the average over auto-correlation functions of the hydrogen-bonding existence functions (either 0 or 1) of all hydrogen bonds (36). Average hydrogen bond lifetimes were measured over the last 10 ns of the simulations of the peptides to understand the effect of each amino acid on hydrogen bond lifetime. In our simulations of SP-$B_{1\text{-}25}$ in 25%-ionized PA monolayers, there are a total of 48 peptides in eight monolayer systems with a wide range of tilt angles. These peptides were categorized according to their individual tilt angles averaged over the last 10 ns of the simulations, without regard to which simulations (i.e., which initial conditions) they were drawn from. We focused on three different ranges: 29° ~ 39°, 51° ~ 57°, and 81° ~ 86°. In each range of the tilt angle, 5 ~ 8 peptides were sampled from 4 ~ 5 different simulations with 25%-ionized PA monolayers.

Fig. 9 shows the average hydrogen bond lifetimes of each amino acid in the sampled peptides. Arginine and lysine have cationic side chains and form strong hydrogen bonds with the anionic headgroups of ionized PA molecules. Therefore, each residue of R-12 and R-17 has almost equally long hydrogen bond lifetimes for any range of the tilt angles, suggesting that those arginine residues play an important role in anchoring the peptide in the monolayer. Whereas R-12 and R-17 have long hydrogen bond lifetimes, K-16 and K-24 have relatively shorter hydrogen bond lifetimes, apparently because of frequent breaking and reformation of hydrogen bonds, which was shown in Fig. 7 *b*. On the other hand, Fig. 9 shows that each residue of Y-7 and Q-19 has longer hydrogen bond lifetimes when the peptide tilt angle is in the ranges of 51° ~ 57° and 81° ~ 86° than for smaller tilt angles. This apparently occurs because Y-7 and Q-19, when in less tilted peptides (relative to the perpendicular orientation), are less accessible to the monolayer. Since anchoring of the peptide to the monolayer occurs whether or not Y-7 and Q-19 have persistent hydrogen bonds, apparently these residues are less critical to peptide anchoring than are the arginines. However, Y-7 and Q-19 may play an important role in controlling the final orientation of the peptides, since

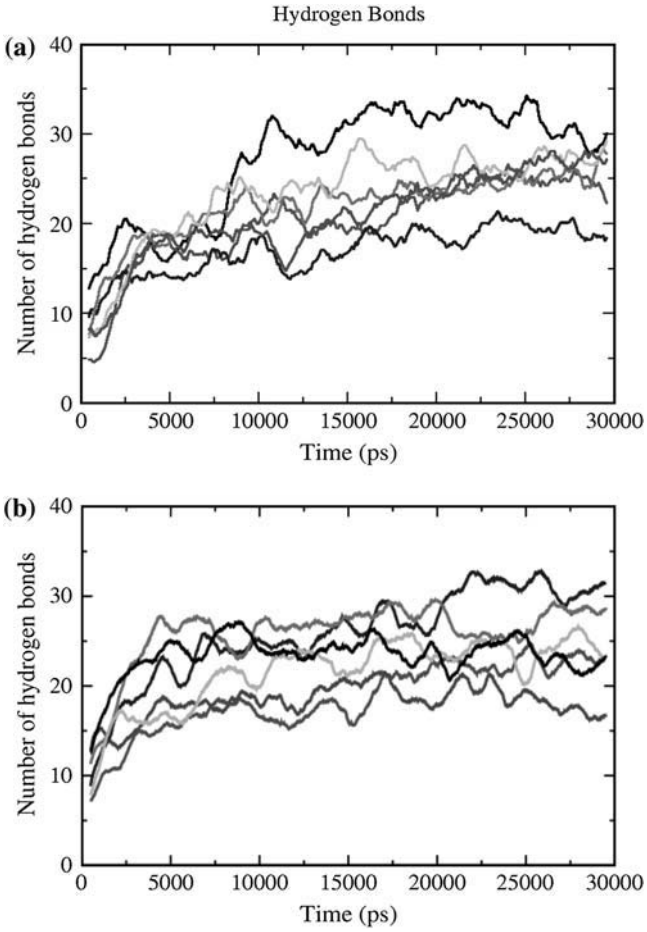

FIGURE 8 Total number of hydrogen bonds formed between SP-B_{1-25} and PA in SPB2 as a function of time for (*a*) SPB2 (initially perpendicular peptide) and (*b*) SPB7 (initially horizontal peptide). Each line represents an individual peptide in the monolayer.

these residues can gain more persistent hydrogen bonds when the peptide is more nearly parallel to the monolayer.

The effect of individual amino acids on the conformation of mutated SP-B_{1-25}

We performed simulations of three mutated peptides (SPB2-MUT1–SPB2-MUT3). Table 5 shows the amino acid sequences of the mutated peptides. In SPB2-MUT1, Y-7 and Q-19 are replaced by alanine to observe if they are important for tilting the peptide, which was discussed in the analysis of hydrogen bonds. In SPB2-MUT2, all the arginines and lysines, R-12, K-16, R-17, and K-24, are replaced by alanines to remove the charged residues that were observed to be important for anchoring the peptide into the monolayer. In SPB2-MUT3, all the residues with hydrogen bond donors in their side chain are replaced by alanines.

Fig. 10 shows the average position of the PA headgroup carbons and the backbone carbons of R-12 residues for the three peptides in each monolayer over the whole simulation.

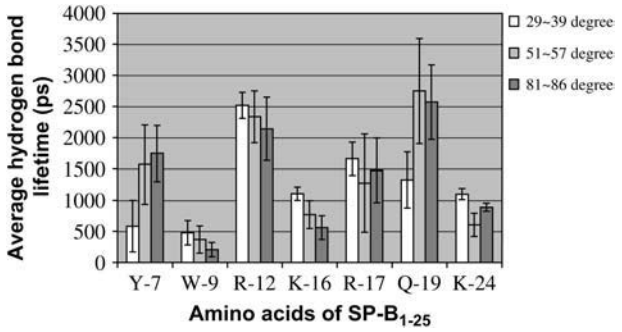

FIGURE 9 Average hydrogen bond lifetimes of each amino acid residue in the peptides, categorized according to the range of tilt angles shown.

Although the centers of mass of the C_α atoms of the R-12 residues in SPB2 and SPB2-MUT1 are positioned close to the center of mass of the PA headgroup carbons, the centers of mass of the C_α atoms of the A-12 residues in SPB2-MUT2 and SPB2-MUT3 are positioned more deeply inside the tail region of the PA monolayer, showing that the peptides in SPB2-MUT2 and SPB2-MUT3 are more deeply inserted into the tail region of the PA monolayer when arginine at position 12 is replaced by alanine. This result suggests that the interactions between charged residues of the peptide and the headgroups of PA play an important role in anchoring the peptides in the PA monolayers, supporting the conclusions we drew from the hydrogen-bonding analysis. Table 6 shows the number of hydrogen bonds of all six mutated SP-B_{1-25} peptides averaged over the last 10 ns of the simulations. From this, we see that the hydrogen bond interactions of the charged residues are much more numerous than those of the uncharged residues; i.e., SPB2-MUT2 and SPB2-MUT3 have fewer hydrogen bonds than do SPB2 and SPB2-MUT1. These results show that charged residues of the peptide dominate the hydrogen-bonding interactions between the peptide and the PA headgroups, anchoring the peptides to the headgroup of PA.

Tilt angles of the mutated peptides were analyzed to understand the effects of Y-7 and Q-19 on the tilting of the peptide and the influence of hydrogen bonding on the tilt. Table 7 shows average tilt angles of the mutated peptides averaged over the last 10 ns of the simulations. Note that the average tilt angle of SPB2-MUT1 is 39°, which is much less than the average tilt angle of SPB2, which is 62°, showing

TABLE 5 Sequences of mutated SP-B_{1-25}

Name	Sequence
SPB2	FPIPL PYCWL CRALI KRIQA MIPKG
SPB2-MUT1	FPIPL PACWL CRALI KRIAA MIPKG
SPB2-MUT2	FPIPL PYCWL CAALI AAIQA MIPAG
SPB2-MUT3	FPIPL PACAL CAALI AAIAA MIPAG

In SPB2-MUT1, Y-7 and Q-19 are replaced with alanine. In SPB2-MUT2, R-12, K-16, R-17, and K-24 are replaced with alanine. In SPB2-MUT3, all the residues having hydrogen-bond are replaced with alanine.

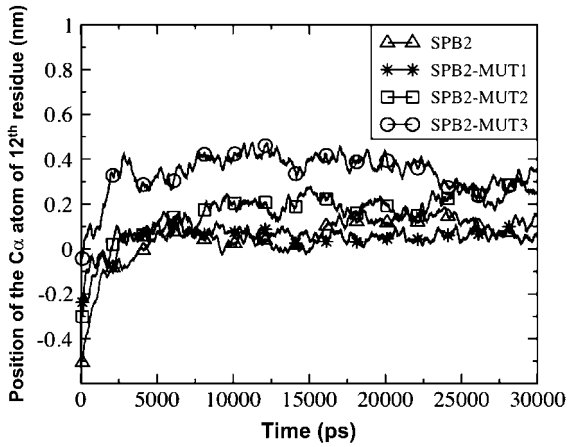

FIGURE 10 The average distance between center of mass of the C_α atoms of R-12 or A-12 residues and center of mass of PA headgroup carbons in SPB2, SPB2-MUT1, SPB2-MUT2, and SPB2-MUT3. Center of mass of PA headgroup carbons is fixed at the point 0 in the *y* axis. When C_α atoms of the 12th residue migrate toward the tail region of the monolayer, the distance between the C_α atoms of the 12th residue and PA headgroup carbons becomes positive. Migration toward the water yields a negative distance.

that Y-7 and Q-19 do play an important role in tilting the peptides in the monolayers, which confirms the conclusion drawn from the analysis of hydrogen bond lifetimes. Note also that the tilt angles of SPB2-MUT1 encompass a broad range of values, 16–81°. The average tilt angles of the six individual peptides in SPB2-MUT1 are 16°, 17°, 22°, 35°, 66°, and 81°. For the two peptides having higher tilt angles of 66° and 81°, the backbones of the alanine counterparts of Y-7 have 0.8 and 1.04 hydrogen bonds, respectively, and the backbones of the alanine counterparts of Q-19 have 0.8 and 0.9 hydrogen bonds, whereas in the four peptides with lower tilt angles, these numbers of hydrogen bonds are lower, ranging from 0.05 to 0.75 backbone hydrogen bonds in the alanine counterparts to Y-7 and from 0 to 0.43 backbone hydrogen bonds in the counterparts of Q-19. This difference suggests that the hydrogen bond interactions between backbones of the mutated peptides and PA are correlated with the tilting of the mutated peptide. This effect on tilt

TABLE 7 Average tilt angles of mutated SP-$B_{1\text{-}25}$ averaged over the time period 20 ns–30 ns for each of six molecules in each system (column 2), and over all six molecules over this period (column 3)

	Range of tilt angle (°)	Average tilt angle (°)
SPB2	37 ~ 77	62
SPB2-MUT1	16 ~ 81	39
SPB2-MUT2	32 ~ 83	58
SPB2-MUT3	32 ~ 85	58

angle of hydrogen bonding of backbone atoms is more pronounced in SPB2-MUT1 than in the unmutated peptide because the bulky side chains of tyrosine and glutamine in the latter are replaced by a much smaller side chain, alanine, in the former, which makes the headgroup of PA more accessible to the backbones of the SPB2-MUT1 peptide. Table 6 shows that the alanine counterpart of the α-helical Q-19 has more backbone hydrogen bonds in the mutated peptide than does Q-19 in the unmutated peptide. Presumably, this occurs because the introduction of alanine in place of Q-19 breaks the α-helical structure of the latter, freeing up the backbone atoms that are involved in forming the α-helix in Q-19 and allowing them to form hydrogen bonds with PA headgroups in the alanine mutant. However, when Y-7 is replaced by alanine, the number of backbone hydrogen bonds does not increase as much as occurs when Q-19 is replaced by alanine because Y-7 and the alanine counterpart of Y-7 are both coil-forming peptides, which makes the headgroup of PA accessible to the hydrogen-bond-forming backbone atoms of both mutated and unmutated peptides. To sum up, although in the unmutated peptide SPB2 the hydrogen bonds with side chains of Y-7 and Q-19 help orient the peptide parallel to the interface, when these amino acids are replaced by alanines, which cannot form side-chain hydrogen bonds, the peptide backbone becomes more accessible to hydrogen bonding with the headgroup of the PA, and this can also help orient the peptide parallel to the interface for some of the peptides. However, the majority of the peptides (four out of six) fail to form these backbone hydrogen bonds and remain oriented more nearly

TABLE 6 Average number of hydrogen bonds of mutated SP-$B_{1\text{-}25}$ averaged over the time period 20–30 ns for all six molecules in each system

	Average number of hydrogen bonds									
	Backbones			Side chains						
	Y-7	Q-19	9th ~ 25th	Y-7	W-9	R-12	K-16	R-17	Q-19	K-24
SPB2	0.4	0.0	8.7	0.5	0.3	2.7	1.3	1.3	1.1	1.3
SPB2-MUT1	0.5	0.4	10.3	-	0.1	2.9	1.1	2.2	-	1.1
SPB2-MUT2	0.4	0.4	11.1	1.1	0.1	-	-	-	1.3	-
SPB2-MUT3	0.5	0.4	12.9	-	-	-	-	-	-	-

The numbers of hydrogen bonds were categorized as either backbone donors and acceptors (columns 2, 3, and 4) or side-chain hydrogen bond donors (columns 5–11). The residues are named based on the SPB2 structure; in the mutants, alanines replace some of these residues, as indicated in Table 5. Backbone hydrogen bonds are divided into those involving Y-7 and Q-19 or their alanine counterparts in SPB2-MUT1 and SPB2-MUT3 (columns 2 and 3), and the remaining residues (column 4), which form an α-helical structure.

perpendicularly to the interface. Thus, the side-chain hydrogen bonds in the unmutated Y-7 and Q-19 more reliably anchor the peptide in a highly tilted orientation than do the backbone hydrogen bonds in the alanine-containing mutants.

The effect of each amino acid residue of SP-B_{1-25} on the conformation of the peptide in the PA monolayer can provide atomic-scale insights into the electrostatic interactions between the peptide and the PA monolayer. Although pure anionic PG and PA, which are important for the adsorption and respreading of DPPC, have relatively low collapse pressures relative to DPPC, it was observed experimentally that both SP-B and SP-B_{1-25} increase the collapse pressure of the PA monolayer to nearly 70 mN/m, which can be maintained in the absence of the peptide only by a monolayer of pure DPPC. Longo et al. (31) found that an uncharged mutant of SP-B was not able to increase the collapse pressure of the PA monolayer, suggesting that specific charge interaction between the anionic PA and the cationic protein is important for the monolayer stabilization. In our simulations, electrostatic interactions between PA and SP-B_{1-25} were investigated by a hydrogen bond analysis, which shows that the charge interactions between R-12 and R-17 with anionic PA play an important role in anchoring the peptide into the interface between the monolayer and water, and the interactions between Y-7 and Q-19 with PA are critical to control the tilt of the peptide in the monolayer. The simulations showing the anchoring effect of arginine residues thus complement the experimental results by indicating which residues control peptide tilting.

CONCLUSIONS

MD simulations of 20 wt % LS peptide fragment SP-B_{1-25} in PA monolayers were performed for 30 ns under various conditions to understand the interactions between the peptide and the monolayer and to test the ability of simulations to predict experimentally measured peptide-monolayer properties. We varied the surface area of the PA, the extent of PA ionization, and initial configurations of the peptides. We found that the PA monolayer is partially disordered by the presence of the peptide in that PA molecules both adjacent and (to a lesser extent) nonadjacent to the peptides suffer a reduction in tail order parameters, and the headgroup region of the peptide is broadened, as some PA molecules are pulled out of the monolayer through interactions with peptides. These results are consistent with the experimentally observed peptide-induced fluidization of the PA monolayer. Peptides initially oriented perpendicular to a 25%-ionized PA monolayer tilt to an angle averaging $54° \sim 62°$ with respect to the monolayer normal, which is similar to experimental results from x-ray reflectivity (32). In addition, atomic-scale interactions between the peptide and monolayer were analyzed by hydrogen-bonding analysis of unmutated and mutated peptides, which showed that R-12 and R-17 help anchor the peptide to the monolayer by interacting preferentially with the ionized PA molecules. Y-7 and Q-19 help control the tilt of the peptides in the monolayer through interactions with the PA headgroup.

Although these simulations are able to complement the experimental studies, the small system size and short simulation timescale still limit the extent to which the experimental system can be adequately represented. In particular, it was observed that the formation of strong hydrogen bonds prevents the system from overcoming local minima, which makes it difficult for the equilibrium ensemble to be sampled adequately. In the future, longer runs on larger systems should be attempted, and advanced methods, such as replica exchange MD simulation and coarse-grained MD simulations, should be used to improve sampling.

REFERENCES

1. Schurch, S., J. Goerke, and J. A. Clements. 1978. Direct determination of volume- and time-dependence of alveolar surface tension in excised lungs. *Proc. Natl. Acad. Sci. USA*. 75:3417–3421.
2. Notter, R. H., and J. N. Finkelstein. 1984. Pulmonary surfactant: an interdisciplinary approach. *J. Appl. Physiol.* 57:1613–1624.
3. Shapiro, D. L., and R. H. Notter. 1989. Surfactant Replacement Therapy. Alan R. Liss, New York.
4. Shapiro, D. L. 1980. Respiratory distress syndrome: past, present, and future. *N. Y. State J. Med.* 80:257–259.
5. Notter, R. H., J. N. Finkelstein, and R. D. Taubold. 1983. Comparative adsorption of natural lung surfactant, extracted phospholipids, and artificial phospholipids mixtures to the air-water interface. *Chem. Phys. Lipids*. 33:67–80.
6. Robertson, B. 1983. Lung surfactant for replacement therapy. *Clin. Physiol.* 3:97–110.
7. Pfister, R. H., and R. F. Soll. 2005. New synthetic surfactants: the next generation? *Biol. Neonate*. 87:338–344.
8. Wu, C. W., S. L. Seurynck, K. Y. C. Lee, and A. E. Barron. 2003. Helical peptoid mimics of lung surfactant protein C. *Chem. Biol.* 10:1057–1063.
9. Perez-Gil, J., and K. M. W. Keough. 1998. Interfacial properties of surfactant proteins. *Biochim. Biophys. Acta*. 1408:203–217.
10. Cochrane, C. G., and S. D. Revak. 1991. Pulmonary surfactant protein B (SP-B): structure-function relationships. *Science*. 254:566–568.
11. Oosterlaken-Dijksterhuis, M. A., H. P. Haagsman, L. M. G. van Golde, and R. A. Demel. 1991. Characterization of lipid insertion into monomolecular layers mediated by lung surfactant proteins SP-B and SP-C. *Biochemistry*. 30:10965–10971.
12. Hall, S. B., A. R. Venkitaraman, J. A. Whitsett, B. A. Holm, and R. H. Notter. 1992. Importance of hydrophobic apoproteins as constituents of clinical exogenous surfactants. *Am. Rev. Respir. Dis.* 145:24–60.
13. Yu, S. H., and F. Possmayer. 1990. Role of bovine pulmonary surfactant-associated proteins in the surface-active property of phospholipid mixtures. *Biochim. Biophys. Acta*. 1046:233–241.
14. Yu, S. H., and F. Possmayer. 1992. Effect of pulmonary surfactant B and calcium on phospholipid adsorption and squeeze out of phosphatidylglycerol from phospholipids membranes containing dipalmitoylphosphatidylcholine. *Biochim. Biophys. Acta*. 1126:26–34.
15. Creuwels, L. A. J. M., L. M. G. van Golde, and H. P. Haagsman. 1996. Surfactant protein B: effects on lipid formation and intermembrane lipid flow. *Biochim. Biophys. Acta*. 1285:1–8.
16. Pryhuber, G. S. 1998. Regulation and function of pulmonary surfactant protein B. *Mol. Genet. Metab.* 64:217–228.

17. Nag, K., J. G. Munro, K. Inchley, S. Schurch, N. O. Petersen, and F. Possmayer. 1999. SP-B refining of pulmonary surfactant phospholipids films. *Am. J. Physiol.* 277:L1179–L1189.

18. Piknova, B., W. R. Schief, V. Vogel, B. M. Discher, and S. B. Hall. 2001. Discrepancy between phase behavior of lung surfactant phospholipids and the classical model of surfactant function. *Biophys. J.* 81:2172–2180.

19. Yu, S. H., and F. Possmayer. 2003. Lipid compositional analysis of pulmonary surfactant monolayers and monolayer-associated reservoirs. *J. Lipid Res.* 44:621–629.

20. Schram, V., and S. B. Hall. 2004. SP-B and SP-C alter diffusion in bilayers of pulmonary surfactant. *Biophys. J.* 86:3734–3743.

21. Ballard, P. L., L. M. Nogee, M. F. Beers, R. A. Ballard, B. C. Planer, L. Polk, D. E. deMello, M. A. Moxley, and W. J. Longmore. 1995. Partial deficiency of surfactant protein B in an infant with chronic lung disease. *Pediatrics.* 96:1046–1052.

22. Possmayer, F., K. Nag, K. Rodriguez, R. Qanbar, and S. Schurch. 2001. Surface activity in vitro: role of surfactant proteins. *Comp. Biochem. Physiol. A.* 129:209–220.

23. Clark, J. C., S. E. Wert, C. J. Bachurski, M. T. Stahlman, B. R. Stripp, J. A. Weaver, and J. A. Whitsett. 1995. Targeted disruption of the surfactant protein B gene disrupts surfactant homeostasis, causing respiratory failure in newborn mice. *Proc. Natl. Acad. Sci. USA.* 92:7794–7798.

24. Zaltash, S., M. Palmblad, T. Curstedt, J. Johansson, and B. Persson. 2000. Pulmonary surfactant protein B: a structural model and a functional analogue. *Biochim. Biophys. Acta.* 1466:179–186.

25. Bruni, R., J. Hernandez-Juviel, R. Tanoviceanu, and F. J. Walther. 1998. Synthetic mimics of surfactant proteins B and C: in vivo surface activity and effects on lung compliance in two animal models of surfactant deficiency. *Mol. Genet. Metab.* 63:116–125.

26. Humphrey, W., A. Dalke, and K. Schulten. 1996. VMD: visual molecular dynamics. *J. Mol. Graph.* 14:33–38.

27. Lipp, M. M., K. Y. C. Lee, J. A. Zasadzinski, and A. J. Waring. 1996. Phase and morphology changes in lipid monolayers induced by SP-B protein and its amino-terminal peptide. *Science.* 273:1196–1199.

28. Lipp, M. M., K. Y. C. Lee, A. J. Waring, and J. A. Zasadzinski. 1997. Fluorescence, polarized fluorescence, and Brewster angle microscopy of palmitic acid and lung surfactant protein B monolayers. *Biophys. J.* 72:2783–2804.

29. Cockshutt, A., D. Absolom, and F. Possmayer. 1991. The role of palmitic acid in pulmonary surfactant: enhancement of surface activity and prevention of inhibition by blood proteins. *Biochim. Biophys. Acta.* 1085:248–256.

30. Longo, M. A., A. J. Waring, and J. A. Zasadzinski. 1992. Lipid bilayer surface association of lung surfactant protein SP-B, amphipathic segment detected by flow immunofluorescence. *Biophys. J.* 63:760–773.

31. Longo, M. A., A. M. Bisagno, J. A. Zasadzinski, R. Bruni, and A. J. Waring. 1993. A function of lung surfactant protein SP-B. *Science.* 261:453–456.

32. Lee, K. Y. C., J. Majewski, T. L. Kuhl, P. B. Howes, K. Kjaer, M. M. Lipp, A. J. Waring, J. A. Zasadzinski, and G. S. Smith. 2001. Synchrotron x-ray study of lung surfactant-specific protein SP-B in lipid monolayers. *Biophys. J.* 81:572–585.

33. Kaznessis, Y. N., S. Kim, and R. G. Larson. 2002. Specific mode of interaction between components of model pulmonary surfactants using computer simulations. *J. Mol. Biol.* 322:569–582.

34. Kandasamy, S. K., and R. G. Larson. 2005. Molecular simulation study of the lung surfactant peptide SP-$B_{1–25}$ with DPPC monolayers: insights into interactions and peptide position and orientation. *Biophys. J.* 88:1577–1592.

35. Freites, J. A., Y. Choi, and D. J. Tobias. 2003. Molecular dynamics simulations of a pulmonary surfactant protein B peptide in a lipid monolayer. *Biophys. J.* 84:2169–2180.

36. Berendsen, H. J. C., D. van der Spoel, and R. van Drunen. 1995. GROMACS: a message-passing parallel molecular dynamics implementation. *Comput. Phys. Comm.* 91:43–56.

37. Lindahl, E., B. Hess, and D. van der Spoel. 2001. GROMACS 3.0: a package for molecular simulation and trajectory analysis. *J. Mol. Model.* 7:306–317.

38. Gordon, L. M., K. Y. C. Lee, M. M. Lipp, J. A. Zasadzinski, F. J. Walther, M. A. Sherman, and A. J. Waring. 2000. Conformational mapping of the N-terminal segment of surfactant protein B in lipid using 13C-enhanced Fourier transform infrared spectroscopy (FTIR). *J. Pept. Res.* 55:330–347.

39. Feenstra, K. A., B. Hess, and H. J. C. Berendsen. 1999. Improving efficiency of large time-scale molecular dynamics simulations of hydrogen-rich systems. *J. Comput. Chem.* 20:786–798.

40. Essmann, U., L. Perera, M. L. Berkowitz, T. Darden, H. Lee, and L. G. Pedersen. 1995. A smooth particle mesh Ewald method. *J. Chem. Phys.* 103:8577–8592.

41. Berendsen, H. J. C., J. P. M. Postma, W. F. van Gunsteren, A. Dinola, and J. R. Haak. 1984. Molecular dynamics with coupling to an external bath. *J. Chem. Phys.* 81:3684–3690.

42. Faraldo-Gomez, J. D., G. R. Smith, and M. S. P. Sansom. 2002. Setting up and optimization of membrane protein simulations. *Eur. Biophys. J.* 31:217–227.

43. Sanner, M. F., A. J. Olson, and J. C. Spehner. 1996. Reduced surfaces: an efficient way to compute molecular surfaces. *Biopolymers.* 38:305–320.

44. Hess, B., H. Bekker, H. J. C. Berendsen, and J. G. E. M. Fraaije. 1997. LINCS: a linear constraint solver for molecular simulations. *J. Comput. Chem.* 18:1463–1472.

45. Egberts, E., and H. J. C. Berendsen. 1988. Molecular dynamics simulation of a smectic liquid crystal with atomic detail. *J. Chem. Phys.* 89:3718–3732.

46. Jeffrey, G. A., and W. Saenger. 1991. Hydrogen Bonding in Biological Structures. Springer-Verlag, Berlin.